Physics of the Earth and Planetary Interiors 348 (2024) 107155

Contents lists available at ScienceDirect

Physics of the Earth and Planetary Interiors

journal homepage: www.elsevier.com/locate/pepi

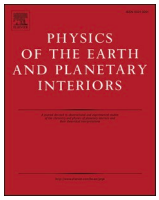

Complexity of the 2016 M 7.8 Kaikōura, New Zealand, earthquake from seismic observation: Inferences of overpressured fluid involvement

Tomomi Okada [a,*], Miu Matsuno [a], Satoshi Matsumoto [b], Yuta Kawamura [b], Yoshihisa Iio [c], Tadashi Sato [a], Ayaka Tagami [a], Satoshi Hirahara [a], Shuutoku Kimura [a], Stephen Bannister [d], John Ristau [d], Martha K. Savage [e], Clifford H. Thurber [f], Richard H. Sibson [g]

[a] Tohoku University, Sendai, Japan
[b] Kyushu University, Nagasaki, Japan
[c] Kyoto University, Uji, Japan
[d] GNS Science, Lower Hutt, New Zealand
[e] Victoria University of Wellington, Wellington, New Zealand
[f] University of Wisconsin-Madison, Madison, United States
[g] University of Otago, Dunedin, New Zealand

ARTICLE INFO

Keywords:
Kaiko¯ura earthquake
Seismic velocity tomography
High seismic velocity
Barrier
High Vp/Vs
Overpressured fluid

ABSTRACT

The M 7.8 Kaikoura earthquake occurred in the northern South Island of New Zealand on 3 Nov., 2016, involving the rupture of >20 faults. To understand the complexity of the Kaikoura earthquake, details of the fault geometry, seismic velocity distribution, and stress field are necessary. We have undertaken seismic tomography along the c. 200 km length of the rupture zone. Data from both 51 temporary stations and 22 permanent (GeoNet) stations were collected from March 2011 to December 2018.

The hypocenter of the Kaikoura earthquake and aftershocks near the Kekerengu fault locate along lineaments where seismic velocity changes laterally in the epicentral region. In the uppermost crust, lower velocities occur beneath the Emu Plain and Cape Campbell. A higher velocity region near Kaikoura may have acted as a barrier that prevented eastward rupture from the hypocenter and led to the complex fault distribution in this area. These complexities in the seismic velocity structure may relate to the multi-segment rupture character of the Kaikoura earthquake. Spatial correlations between rupture areas and high Vp/Vs suggest the involvement of overpressured fluid in the nucleation and propagation of rupture segments, which is also supported by the reactivation of unfavourably oriented strike-slip ruptures, many lying at c.70° to the regional maximum compressive stress trajectories.

1. Introduction

The M 7.8 Kaikōura earthquake occurred in the northern South Island of New Zealand on 3 Nov., 2016 (Fig. 1). New Zealand is located at the plate boundary between the Pacific plate and the Australian plate. The northern South Island is a transition zone between a subduction plate boundary in the north and a strike-slip plate boundary in the south, and complex crustal deformation occurs there (e.g., Wallace et al., 2012; Okada et al., 2019). In the region southeast of the Alpine-Wairau fault, the major right-lateral strike-slip fault in the South Island, there are NE-SW structures sub-parallel to the Alpine-Wairau fault system, including the Awatere, Clarence, Kekerengu, and Hope faults (Figs. 1 and 2). Historic faults have been identified as having been ruptured by earthquakes that produced lateral displacement, such as the 1848 M7.5 earthquake along the Awatere fault, and the 1888 M7.0–7.3 and the 1929 M7.1 earthquakes along the Hope fault. Secondary thrusts have also occurred, especially in the vicinity of the Kaikōura Mountains in the eastern coastal region of the Island (Van Dissen and Yeats, 1991).

From previous studies (e.g., Litchfield et al., 2018; Little et al., 2018; Nicol et al., 2018), the progression of the Kaikōura earthquake is summarized as follows, and names of the following faults are shown in Fig. 3 (b): Initiation of the Kaikōura earthquake occurred at the Humps West fault in the Northern Canterbury Domain (NCD) near the western end of a set of >20 faults that ruptured in the event. Slip propagated eastward

* Corresponding author.
E-mail address: okada.t@tohoku.ac.jp (T. Okada).

https://doi.org/10.1016/j.pepi.2024.107155
Received 3 January 2023; Received in revised form 19 December 2023; Accepted 7 February 2024
Available online 9 February 2024

unilaterally to the Humps East fault and the Leader fault. Slip also occurred on the Conway-Charwell fault and the Stone Jug fault, which have different strike orientations. Slip propagated eastward on the Hundalee fault and the offshore Point Kean fault. Around the Kaikōura Peninsula, the Whites fault also ruptured. Then, slip propagated to the northeast on the Marlborough fault system; e.g., the Upper Kowhai fault, the Manakau fault, the Jordan thrust, and the Kekerengu fault. Slip on the Hope fault was limited to small fault patches. Along the NE-SW striking Kekerengu - Needles fault and the Jordan thrust, horizontal displacement (<10 m) predominated. Faults west (the Fidget) and east (the Papatea) from the Kekerengu fault also slipped. Slip extended offshore on the Needles fault and some small onshore faults (the Lighthouse fault, the Cape Campbell Road fault, and the Marfells Beach fault), then the slip process stopped, and did not extend to other faults (e.g., the Boo Boo fault) south of Cook Strait.

The seismic deformation had a transpressional character combining thrusting and dextral strike-slip. Reverse slip occurred on faults in the NCD south of the Hope fault and dextral slip dominated in the Marlborough faults, although some variations occurred (e.g., large vertical slip on the Papatea fault).

Hamling et al. (2017) constructed a multi-fault model from geodetic data (GNSS and InSAR), the surface trace of the coseismic rupture, and coastal uplift data. The multi-fault rupture was also shown by multiple aftershock alignments (e.g., Lanza et al., 2019; Kawamura et al., 2021). Lanza et al. (2019) used the double-difference hypocenter location technique for their temporay seismic network and found connectivity of the faults of the 2016 Kaikōura earthquake from the aftershock distribution. Chamberlain et al. (2021) further refined the aftershock

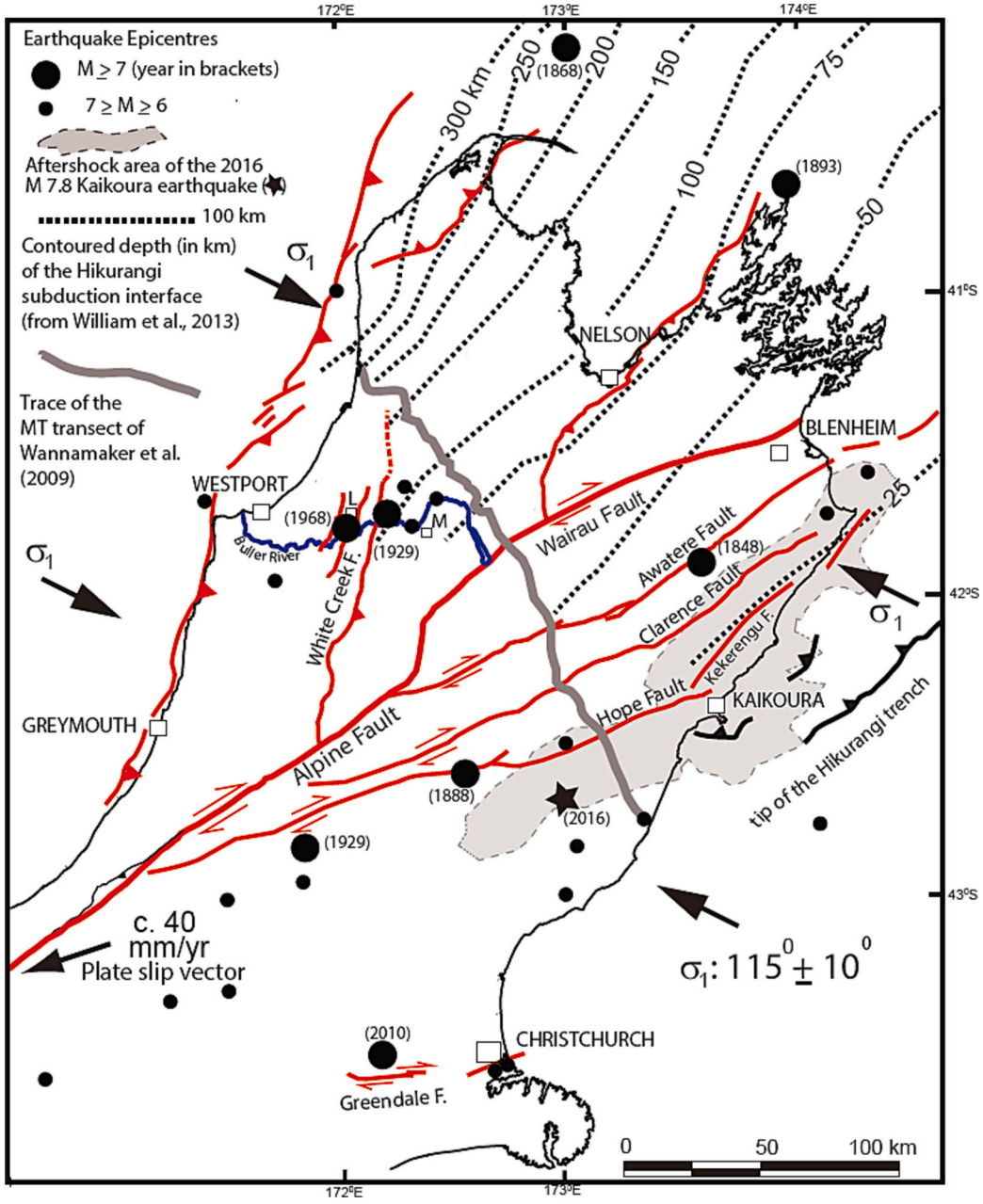

Fig. 1. Tectonic setting: Major Holocene-active fault structures in relation to plate boundary kinematics, the southern termination of the Hikurangi Trench, depth contours on the subducting Pacific slab (from Williams et al., 2013), the course of the Buller River (blue), the inferred contemporary stress field, and the epicentres of large historic earthquakes. Grey bold line denotes the trace of the Wannamaker et al. (2009) magnetotelluric transect. (after Okada et al., 2019). (For interpretation of the references to colour in this figure legend, the reader is referred to the web version of this article.)

locations and seismicity before the mainshock by using matched-filter techniques. Kawamura et al. (2021) used the double-difference hypocenter location technique for their temporary seismic network (Okada et al., 2019), and found over nine faults (aftershock alignments) from the aftershock distribution. Note that the amount of slip on the subducted plate interface is still under debate. Using geodetic data, Hamling et al. (2017) estimated coseismic slip of up to 4 m on the plate interface north or northwest of Kaikōura Peninsula. Bai et al. (2017) estimated coseismic slip of up to 6 m on the plate interface by tsunami waveform modeling with a location similar to that of Hamling et al. (2017). In a different interpretation, Cesca et al. (2017) used joint inversion of seismic and geodetic data to propose a model with a deep thrust fault connecting the shallow faults. Postseismic slip following the Kaikōura earthquake was assumed to occur on the plate interface (e.g., Wallace

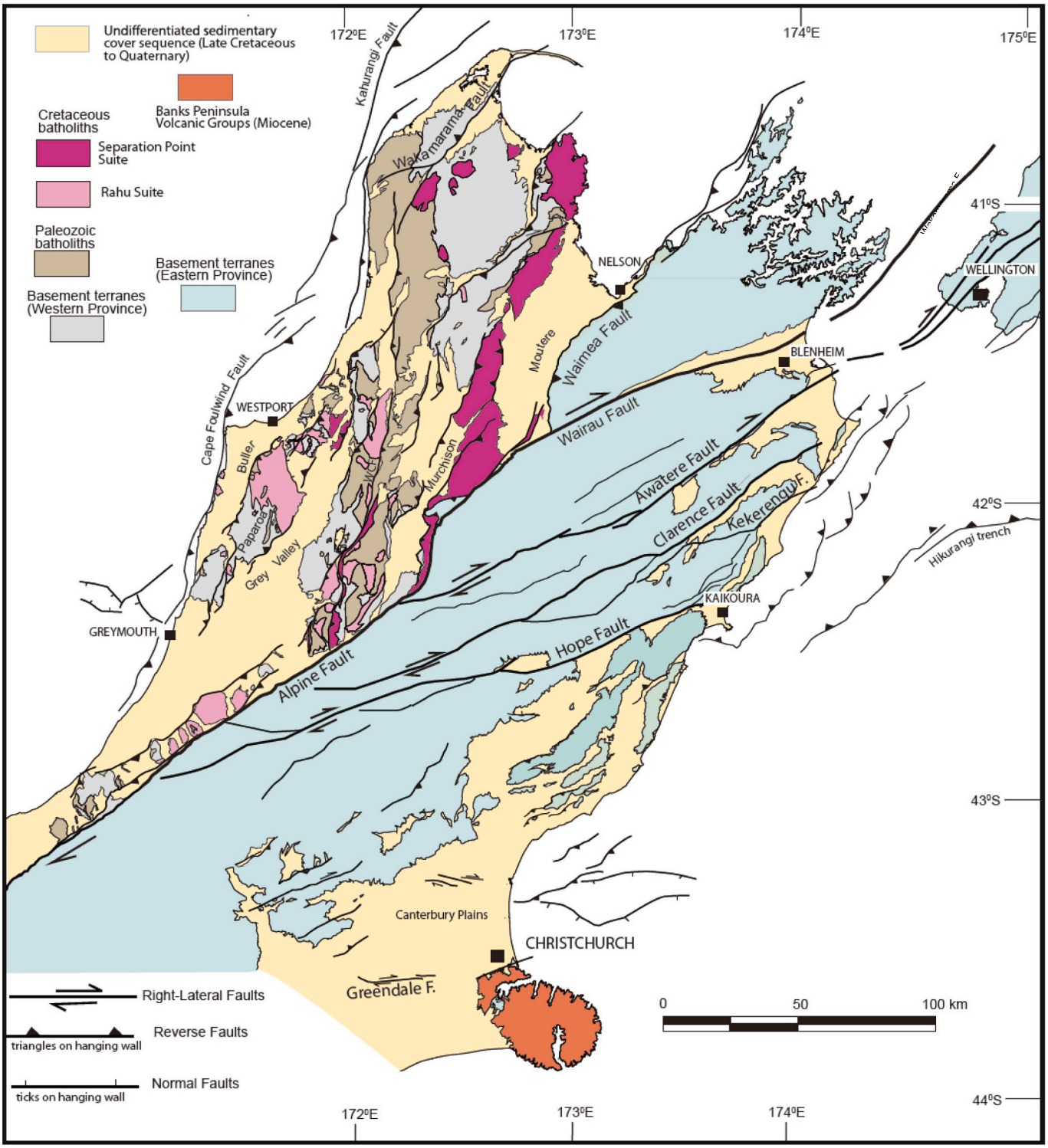

Fig. 2. Tectonic setting: Map of the northern South Island of New Zealand illustrating the crustal geology of the contrasting Buller-Nelson and Marlborough seismotectonic provinces respectively NW and SE of the Alpine-Wairau fault, delineating the principal basement units and the cover sedimentary basins in relation to major fault structures. (after Okada et al., 2019).

et al., 2018).

This multi-fault rupture can be tectonically and physically explained. Van Dissen and Yeats (1991) find a low slip rate along the Hope fault at its eastern end (~10 km), with displacement transferred to the Jordan thrust and other faults such as the Kekerengu fault to the northeast. This slip transfer is also supported by GNSS observations (Wallace et al., 2012). Lamb et al. (2018) suggest that locking on the subduction interface caused the multi-fault rupture of the Kaikōura earthquake. Matsuno et al. (2022) obtained the slip tendency of each fault by using stress tensor inversion results and found a high slip tendency on the western initial fault (the Humps West) and some of other southwestern sub-faults, and low slip tendency on the northern end fault (the Needles) and some of the other northeastern sub-faults. Dynamic rupture modeling can explain the slip propagation process (e.g., Ando and Kaneko, 2018) from the initiation to the end of rupture, but the effect of fluid pressure was not considered in the modeling.

After the earthquake, changes in water levels in wellbores throughout New Zealand were observed (Weaver et al., 2019). Seismic velocity drops of up to 0.5% in the uppermost 2.5 km were observed immediately after the earthquake in the Kaikōura area using ambient noise analysis (Madley et al., 2022), but temporal changes in seismic anisotropy were not resolved in the region (Graham et al., 2020).

Spatial correlation of seismic velocity structure with the size and complexity of earthquakes has been observed for earthquakes in several other places (e.g., Japan; Okada et al., 2007, 2012; Shito et al., 2017 and California; Eberhart-Phillips and Michael, 1993, 1998). In some cases, the lateral extent of a seismic low-velocity area coincides with the aftershock area, suggesting that an area of high fluid content may control the extent of aftershocks in a multi-fault process (Okada et al., 2007). In other cases, high velocity regions correspond to regions of high slip (Okada et al., 2012; Eberhart-Phillips and Michael, 1993, 1998), or of earthquake rupture initiation (Shito et al., 2017). These observations may be explained by larger specific fracture energy (or larger cohesion) in lower deformation and damaged areas with higher seismic velocities (e.g., Aki, 1979). Such areas are expected to store large strains and act as large slip areas (asperities) when they rupture. Additionally, slip behavior is controlled not only by frictional strength but also by medium stiffness (e.g., Ruina, 1983): The higher the seismic wave velocity, i.e., the higher the stiffness, the more difficult it is for the slip to be unstable. Thus, if the strength and/or stability of the area is too great to allow rupture during an earthquake, seismic high-velocity and high-strength/stability area may act as a barrier that stops an earthquake rupture extension (e.g., Aki, 1979).

To further understand the relationship between crustal structure and complex ruptures, it is valuable to obtain the fine structure of the aftershock distribution and three-dimensional velocity structure by using data from a dense seismic station network. Eberhart-Phillips and Bannister (2010) and Eberhart-Phillips et al. (2010) used regional and short-term temporary network seismic data, but we desire to re-determine the seismic velocity structure using data from the 2016 Kaikoura earthquake. Okada et al. (2019) used data from the same seismic network as this study, but the aftershock data that they used was only from the routinely operated stations of the GeoNet and was not well enough located to discuss the relationship between the seismic velocity structure and the Kaikoura earthquake. Heath et al. (2022) used data from the same seismic network as this study, including aftershock data from the Kaikoura earthquake. They adopted a conventional tomography method, but a double-difference procedure could improve both the velocity model and the aftershock locations (Waldhauser and Ellsworth, 2000; Zhang and Thurber, 2003, 2006).

Thus, we have undertaken simultaneous determination of three-dimensional seismic velocity structure and absolute and relative hypocenter relocation along the c. 200 km length of the Kaikōura earthquake rupture zone. We used double-difference seismic tomography with data from a dense network of temporary and permanent seismic stations. Based on our results, we examine the complex hypocenter distribution and compare it with a fault model, features of the seismic velocity distribution that correlate with the spatial extent of total rupture, and some seismic velocity anomalies in and around the Kaikōura peninsula where the most complex rupture occurred during the Kaikōura earthquake.

2. Data and method

Data from both temporary stations (Okada et al., 2019; Lanza et al.,

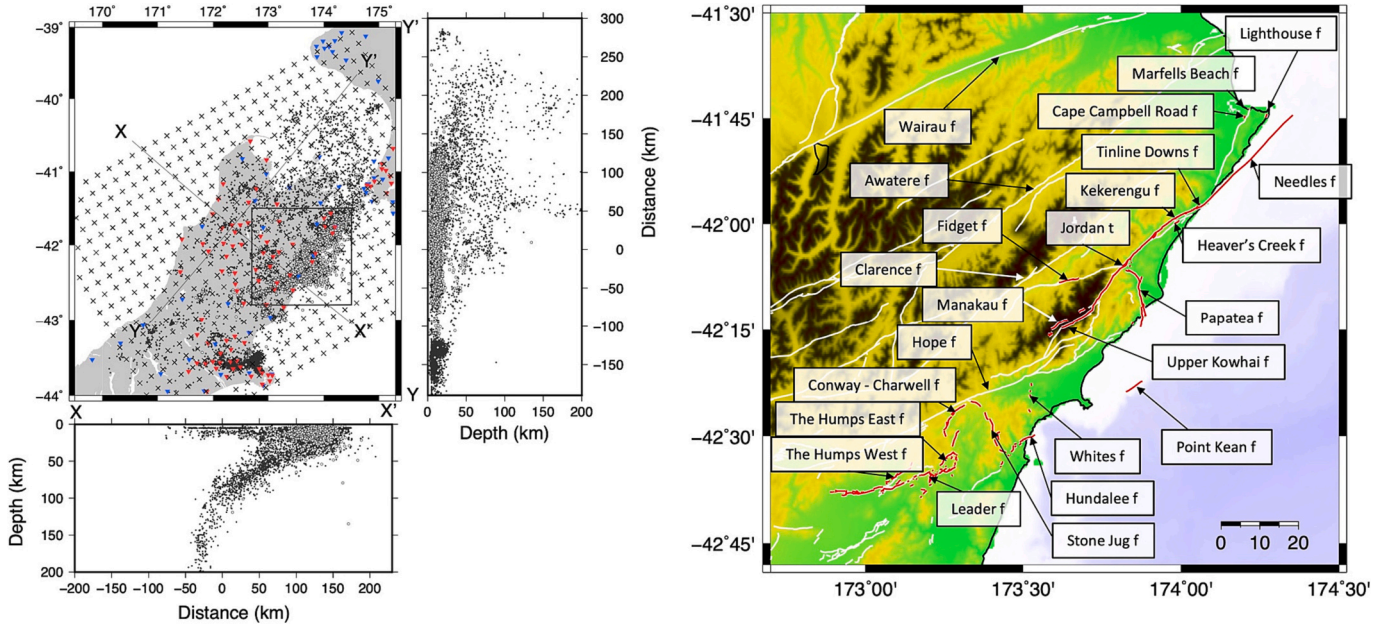

Fig. 3. (Left) Station and seismicity map. Blue and red are permanent (GeoNet) stations and temporary stations, respectively. Circles denote the earthquakes used in this study. (Right) White and red lines are the surface traces s of major faults and the surface rupture of the Kaikoura earthquake from the New Zealand Active Fault Database, GNS Science (2021), respectively. (For interpretation of the references to colour in this figure legend, the reader is referred to the web version of this article.)

2019) and GeoNet stations were collected from March 2011 to December 2018. Earthquakes are from the GeoNet catalog (GNS Science, 2023a, 2023b). GeoNet is a nationwide geophysical observation network in New Zealand. We combine the data set of Okada et al. (2019) with additional arrival time data at temporary stations for aftershocks of the Kaikōura earthquake. We assume no temporal change in the velocity structure before or after the 2016 Kaikōura earthquake, because the reported temporal change was very small ($< 0.5\%$) and limited to the uppermost layer (Madley et al., 2022). The total number of earthquakes used in this analysis is 14,805. Fig. 3 shows the locations of stations and earthquakes used in this study.

Hypocenter locations and the three-dimensional velocity structure were determined using the double-difference tomography method of Zhang and Thurber (2003, 2006). In the double-difference tomography method, we use both absolute arrival times and differential travel times to obtain absolute and relative locations of earthquakes, solving for the three-dimensional seismic velocity structure simultaneously. In this case, we inverted for Vp and Vs, and Vp/Vs was inferred from the Vp and Vs models. The number of absolute times for P and S waves are 495,111 and 319,493, respectively. In this analysis, we used manually and automatically picked arrival times by the method of Horiuchi et al. (1992), which is mainly based on the autoregression model. We used manually picked arrival times of 765 earthquakes with magnitudes greater than about 2.5, which were used in Matsuno et al. (2022). We used automatically picked arrival times of other smaller earthquakes. The estimated uncertainties of arrival times which were automatically picked with Horiuchi's method, were 0.08 s and 0.19 s for P-wave and S-wave, respectively. We applied these uncertainties when we did the checkerboard resolution test. Differential times were calculated for event pairs at an average of 4.6 km offset. The numbers of differential travel times for P and S waves are 4,698,311 and 2,961,261, respectively. The initial seismic velocity structure for seismic velocity tomography is from the New Zealand nation-wide velocity model by Eberhart-Phillips et al. (2010), which was derived from seismic tomography studies at regional scale. We used a grid with an interval of 20 km horizontally and depth nodes at −1, 3, 8, 15, 23, 30, 38, 48, 65, 85, 105, 130, 155, 185, and 225 km depth. The horizontal grid interval was determined through the checkboard test. The vertical grid was the same as Eberhart-Phillips et al. (2010). The initial seismic velocity at each grid was resampled from Eberhart-Phillips et al. (2010). The smoothing parameters were determined as 600 for Vp and 20 for Vs so that the obtained seismic velocity structure has a stable Vp/Vs resolution. The damping factors were determined so that the appropriate condition numbers (about 40 to 80; c.f., Waldhauser, 2001) for being a well-conditioned damped least square problem during the inversion are obtained. The parameter set for the double-difference tomography is shown in Tables S1 and S2.

Arrival time RMS is reduced from 0.98 s to 0.22 s with the revised velocity model (Fig. S1). Fig. 4 (and Figs. S2 and S3) show the results of a checkerboard resolution test. For the test, we added Gaussian random noise with a standard deviation of 0.08 s for the P-wave and 0.19 s for the S-wave, which correspond to the arrival time uncertainties by the automated picking, to all the true arrival times. The checkerboard resolution test was done for Vp and Vs, and Vp/Vs was inferred from Vp and Vs using the same procedure for the real data. We used a checkerboard pattern with a perturbation of $+-5\%$ for the P-wave and $-+$ (opposite sign for P-wave) for S-wave, respectively. We obtained a Vp/Vs structure that is reliable at a scale of about 20–40 km based on the checkerboard

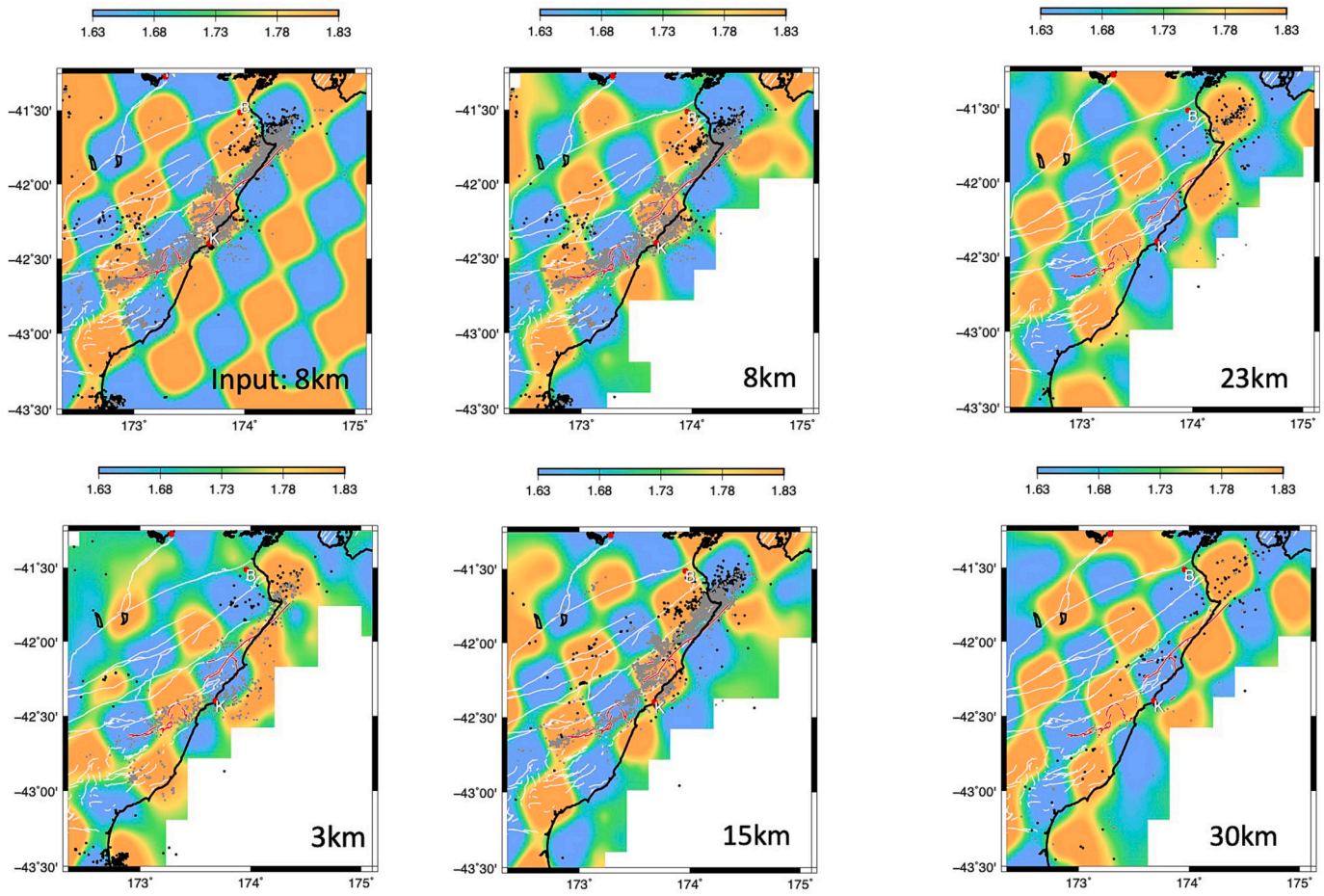

Fig. 4. Result of the checkerboard resolution test. Vp/Vs at depths of 3, 8, 15, 23, 30 km are shown. See Fig. S3 for Vp test.

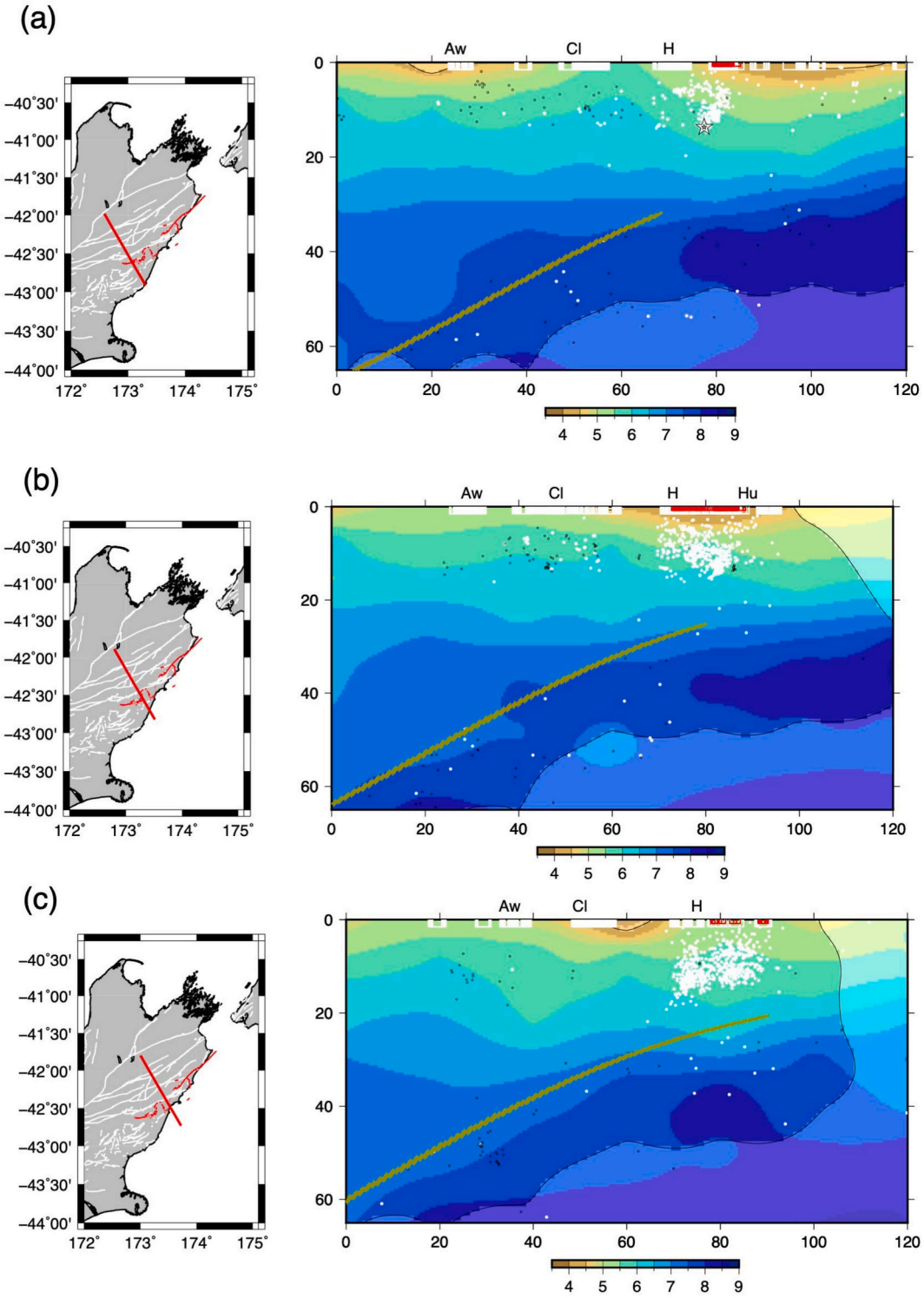

Fig. 5. Cross-sections of Vp (km/s); (a) through the hypocenter of the Kaikoura earthquake, which is shown by a white star, (b) NE of the hypocenter of the Kaikoura earthquake, (c) through the Hundalee-Whites-Hope faults, (d) through Kaikoura Peninsula, (e) through the Jordan Thrust, the Kekerengu and Papatea faults, (f) through the Kekerengu area and (g) through the Needles fault. In (a), the white star denotes the hypocenter of the Kaikoura earthquake. Black and white dots denote earthquakes before and after the Kaikoura earthquake, respectively. The sand colored line shows the plate interface of Williams et al. (2013). White and red boxes near the surface are the locations of major faults and the surface traces of coseismic rupture from the New Zealand Active Fault Database, GNS Science (2021), respectively; Wr: Wairau, Aw: Awatere, Cl: Clarence, H: Hope, CC: Conway-Charwell, SJ: Stone Jog, HE: the Humps East, Fg: Fidget, Mk: Manukau, UK: Upper Kowhai, Kk-JT: Kekerengu-Jordan Thrust, Pa: Papatea, Lh: London Hill, Lt: Lighthouse, Ne: Needles fault. The lighter shading area below the black line represents the area that is least well-resolved in the tomographic inversion. (For interpretation of the references to colour in this figure legend, the reader is referred to the web version of this article.)

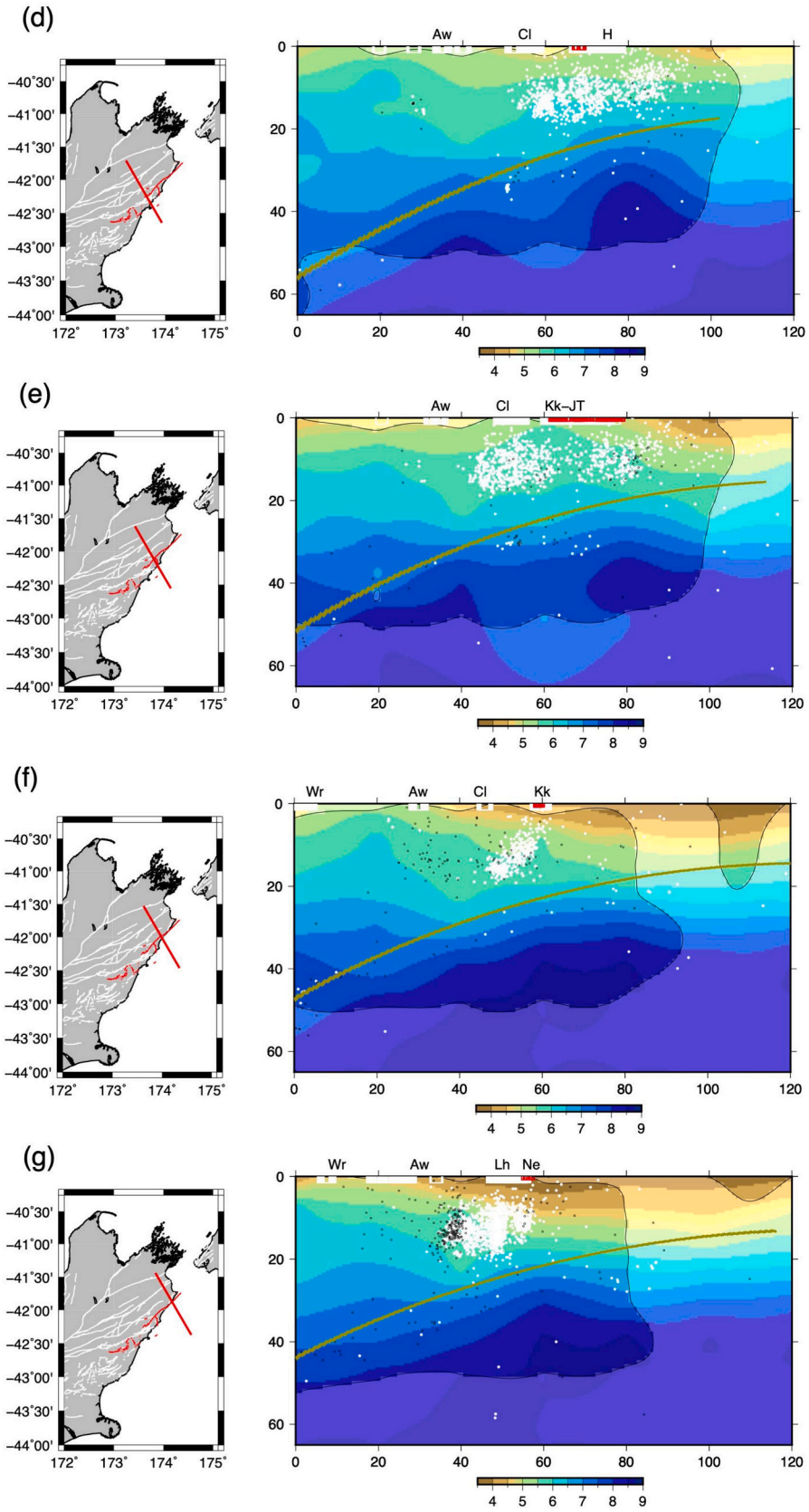

Fig. 5. (*continued*).

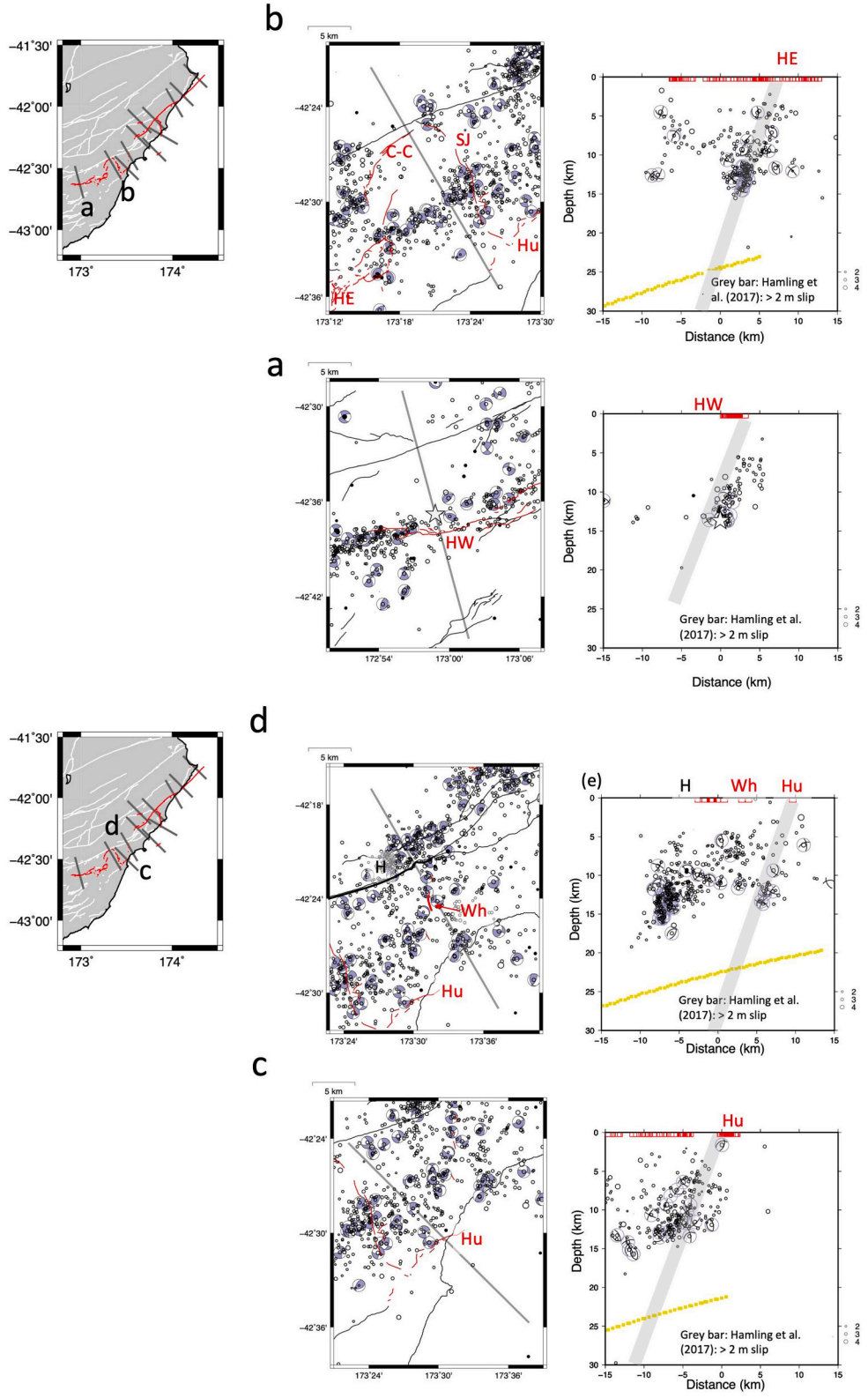

Fig. 6. Map view of hypocenters. Size of circle is proportional to the magnitude as the example shown in the right-bottom of the cross section. Focal mechanisms by Matsuno et al. (2022) are also shown. Black and red lines are surface trace of major faults and coseismic rupture, respectively. Name of each fault is shown as in Fig. 3. Bold line shows the location of the cross section. Cross section of relocated hypocenters within 5 km along the bold line in map views. Star in (a) denotes the hypocenter of the Kaikoura earthquake. Red boxes denote the surface traces of coseismic rupture from New Zealand Active Fault Database, GNS Science (2021). Grey bar is the fault with slip of over 2 m determined by Hamling et al. (2017). In (g), Grey broken bar is the Point Kean fault (Clark et al., 2017). Yellow broken line shows the plate interface of Williams et al. (2013). (For interpretation of the references to colour in this figure legend, the reader is referred to the web version of this article.)

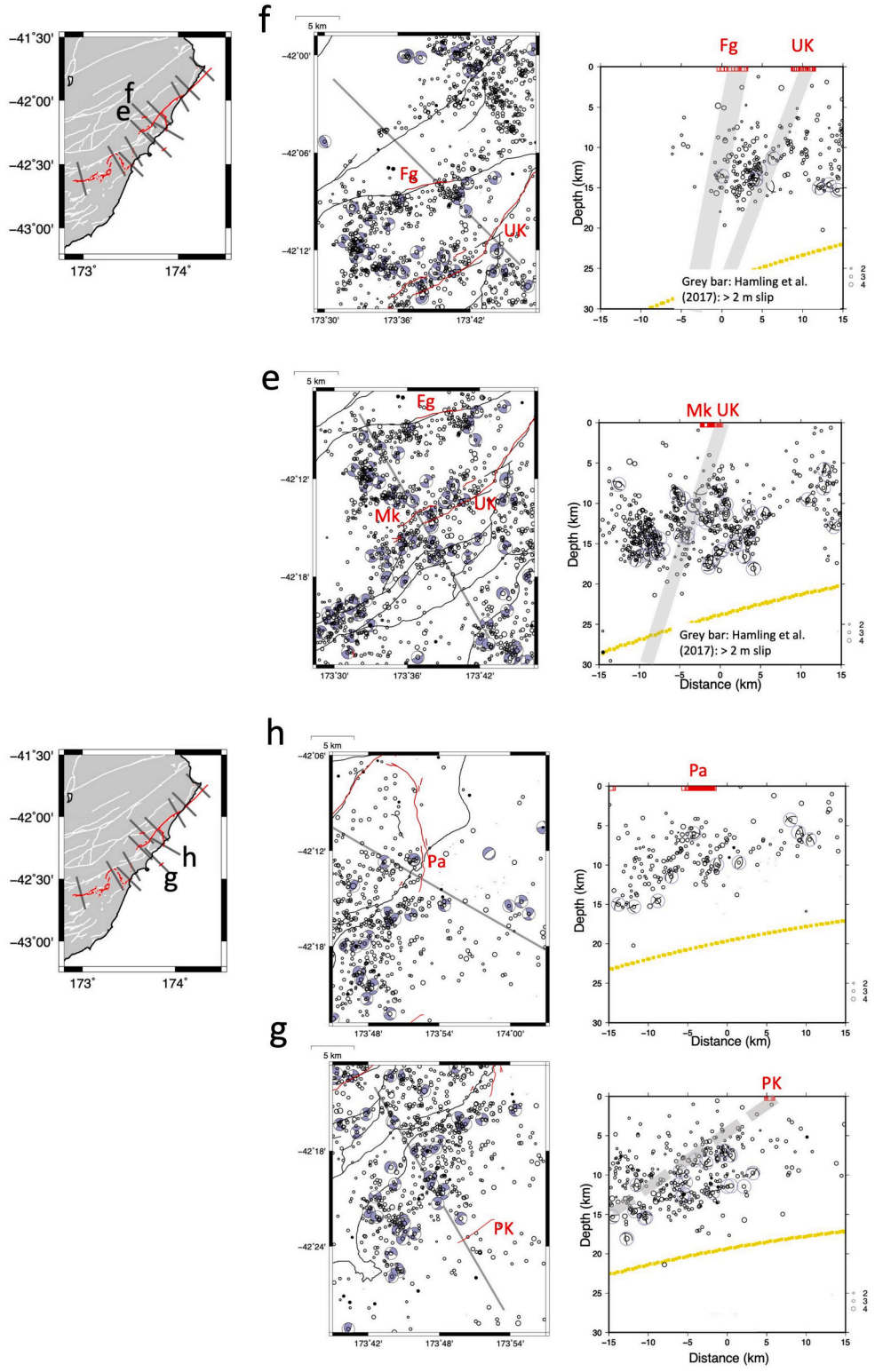

Fig. 6. (*continued*).

test. The checkerboard resolution test showed the arrival uncertainties did not significantly bias the result. The pattern was recovered in the aftershock area, even along the coastline. We obtained images in the eastern coastal area by including source-receiver pairs with ray paths along the shoreline with various lengths, although some smearing occurred for the offshore area.

3. Results

As the surface fault distribution, seismic velocity structure and aftershock distribution change laterally through the focal area, we show cross-sections, approximately normal to the main faults from the hypocenter of the Kaikoura earthquake to the northern end of the rupture area. Fig. 5 shows vertical cross-sections of the tomography result for

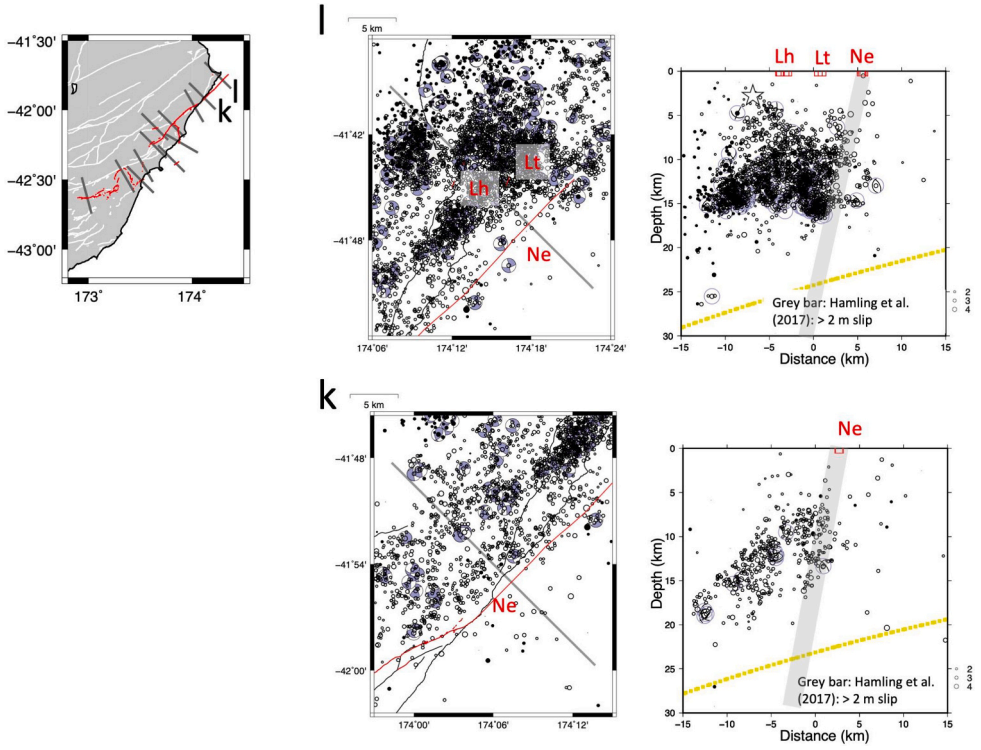

Fig. 6. (*continued*).

Vp. We also show the aftershock distribution determined by the double-difference relocations while revising the three-dimensional seismic velocity structure. We estimated the location uncertainties by the differences between the true locations and the obtained locations in the checkerboard resolution (reconstruction) test (c.f., Zhang and Thurber, 2003), yielding an average value of about 0.30 km horizontally and 0.63 km vertically. Most aftershocks are above a depth of about 20 km and are shallower than the plate interface of Williams et al. (2013). Most are also distributed in a Vp range of 5 km/s to 6 km/s.

Seismic high-velocity zones are observed below the Williams et al. (2013) plate interface for multiple cross-sections of Fig. 5. These seismic high-velocity zones likely correspond with the subducted Pacific Plate. We also see some slab seismicity below the plate interface.

Fig. 5 (a) is the cross-section through the hypocenter of the Kaikōura earthquake. The hypocenter is located beneath the northern margin of a basin-like low velocity uppermost layer.

The cross-section near the Conway-Charwell fault is shown in Fig. 5 (b). Aftershocks are distributed below the low velocity uppermost layer.

Near the Hundalee fault, aftershocks are distributed southeast of the low velocity uppermost layer (Fig. 5 (c)).

Near Kaikōura, the shallowest low-velocity region is not as extensive (Fig. 5 (d)). Most aftershocks are located at depths <20 km and are ~5 km shallower than the subduction interface of Williams et al. (2013).

Fig. 5 (e) shows the cross-section across the Jordan thrust and along the Papatea fault. The shallowest low-velocity region is not as deep in this area, in particular, in and around the Jordan thrust or Kekerengu fault.

The cross-section across the Kekerengu fault is shown in Fig. 5(f). Aftershocks near the Kekerengu fault locate where the thickness of the shallowest low seismic velocity region changes laterally.

The shallowest low-velocity area is very broad near the Needles fault (Fig. 5 (g)).

Vertical cross-sections of the aftershock distribution from SW to NE, i.e., from the hypocenter to the northern end of the entire rupture area, are shown in Fig. 6, along with the focal mechanisms by Matsuno et al. (2022). We show the fault model of Hamling et al. (2017), which is one of the most referenced fault models of the Kaikoura earthquake, at each cross-section for reference. In Fig. S4, we also compared the model of Mouslopoulou et al. (2019) for an additional reference. Matsuno et al. (2022) suggested that many of the aftershocks occurred off-fault, from an analysis using the Kagan angle. Some of the focal mechanisms are consistent with the corresponding fault, but others are not.

Fig. 6 (a) is the westernmost cross-section through the hypocenter of the Kaikōura earthquake. Here, aftershock alignments near the Kaikōura mainshock appear north- and northwestward-dipping and well-aligned on the corresponding sub-fault (the Humps fault) of the Hamling et al. (2017) model. Some of the aftershocks are consistent with a sub-fault by Mouslopoulou et al. (2019) (Fig. S4 (a)).

East of the hypocenter,; the cross-section near the Conway-Charwell fault shows a complex fault distribution (Fig. 6 (b)). There is a clear ENE-WSW alignment of seismicity connecting the Humps East fault and the Stone Jog fault. Focal mechanisms are also strike-slip and reverse types. There are almost no aftershocks on the plate interface fault at a depth of 20 km to 30 km (Fig. S4 (b)).

Further east, Fig. 6 (c) and (d) show the cross-sections near the Hundalee fault. In Fig. 6 (c), aftershocks are distributed around the sub faults corresponding to the Hundalee fault, but they suggest a shallower dip and shallower cut-off at depth than the Hamling et al. (2017) model. In Fig. 6 (d), some aftershocks are near the Whites fault. Many aftershocks appear NW of the Hope fault. There are almost no aftershocks on the plate interface fault at a depth of about 25 km (Fig. S4 (d)).

Near the Kaikoura Peninsula, the trend of the strikes of the fault and the aftershock alignment changed anticlockwise from about ENE-WSW to NE-SW(Fig. 6 (e), (f) and (g)). In Fig. 6 (e) and (f), onshore aftershocks form clusters and are distributed around the Upper Kohwai fault, the Manukau fault, and a few aftershocks occur beneath the Fidget fault. Most focal mechanisms are right-lateral slip, assuming a NE-SW fault plane. In Fig. 6 (g), offshore aftershocks are mainly distributed to the west of the surface trace of the Point Kean fault (Clark et al., 2017) (or the Kaikōura Peninsula fault), and on and around the Offshore Splay Thrust Fault (OSTF) by Mouslopoulou et al. (2019) (Fig. S4 (g)).

About the central part of the entire rupture area, Fig. 6 (i) and (h)

show the cross-sections across the Jordan thrust and along the Papatea fault. One interesting alignment appears to be perpendicular to the Jordan thrust or the Kekerengu fault and to the northwest extension of the Papatea fault (Fig. 6 (i)). The aftershocks occurred in the southwest (hanging wall side) of the surface trace of the Papatea fault. There is a northwestward dipping aftershock distribution at the southern end of the Papatea fault (Fig. 6 (h)). This distribution is on and around the OSTF and the Papatea fault by Mouslopoulou et al. (2019) (Fig. S4 (h)).

Distinct slip occurred along the Kekerengu fault (e.g., Hamling et al., 2017). Fig. 6(j) shows the cross-section across the Kekerengu fault. Most focal mechanisms are right-lateral slip, assuming a NE-SW fault plane (Fig. 6j). Aftershocks near the Kekerengu fault are distributed in an alignment with northwestward dip and reasonably well-located on the corresponding sub-fault of the Hamling et al. (2017) model, except that they have a shallower dip (Fig. 6 (j)). The OSTF by Mouslopoulou et al. (2019) extends to this cross-section but there are no aftershocks on or around it (Fig. S5 (h)).

In the northern end of the entire rupture area, Fig. 6 (k) and (l) show the cross-sections across the Needles fault. In Fig. 6 (k), some aftershocks are distributed along the Needles fault. In Fig. 6 (l) (see also Fig. S5), aftershocks are distributed northwest of the Needles faults, and along the Lighthouse and London Hill faults. The aftershocks of the 2013 Lake Grassmere earthquake are located at the northwestern margin of the aftershock area of the 2016 Kaikōura earthquake.

In the uppermost crust, as shown in Fig. 7(a), lower velocities occur beneath the basins in Emu Plain and at Cape Campbell. In the western end of the rupture area, the coseismic fault and aftershocks are distributed at the northern margin of the low-Vp area. Higher velocities over 5 km/s occur in and around Kaikōura, where there are mountains.

Fig. 7 (b) is the map view of Vp at a depth of 15 km. Higher velocity of over 6 km/s can be seen approximately in and around Kaikōura. In this higher velocity area, the aftershock distribution is complex and forms many alignments.

Vp/Vs are inhomogeneously distributed as shown in Fig. 8, map views of Vp/Vs at depths of 8, 15, 23, and 30 km. At a depth of 8 km, distinct high Vp/Vs (> about 1.80) is present near the hypocenter, below Kaikōura Peninsula, and below Cape Campbell. At a depth of 15 km, distinct high Vp/Vs zones are observed below Kaikōura Peninsula and below Cape Campbell. At a depth of 23 km (the middle to lower crust, below the aftershock area), high Vp/Vs occurs not only near the hypocenter but also along the northern part of the rupture zone up to Cape Campbell. At a depth of 30 km, high Vp/Vs is seen below Kaikōura Peninsula, below Cape Campbell, and west of the aftershock area, i.e., above the possible coseismic slip area on the plate interface (approximately from Hamling et al., 2017) and the postseismic slip area on the plate interface (approximately from Wallace et al., 2018), although the existence of coseismic slip on the plate interface is controversial (e.g., Cesca et al., 2017).

The inhomogenous distribution of Vp/Vs is seen in the cross-section of Vp/Vs across the Kaikōura Peninsula (Fig. 9). In this area, high Vp/Vs

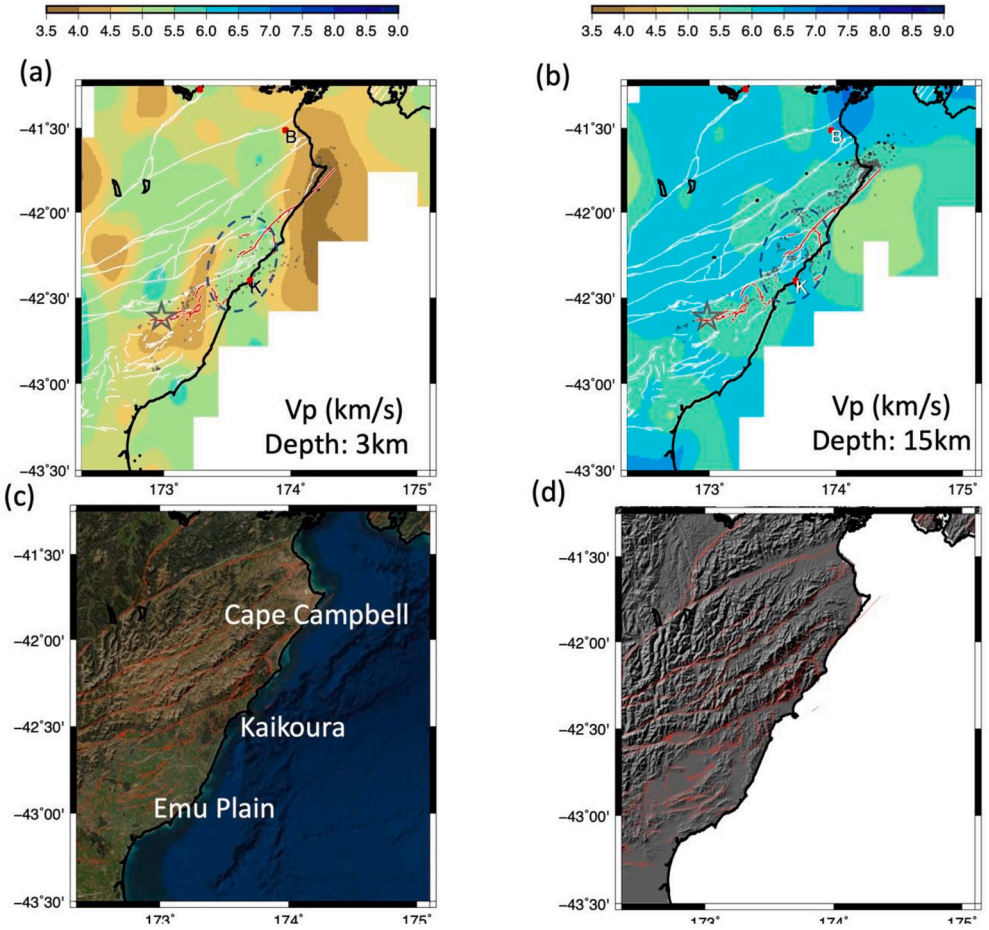

Fig. 7. (a) Map view of Vp at a depth of 3 km. White and red lines denote surface trace of major faults and coseismic faults, respectively. Grey and black dots are the earthquakes (M ≥ 4.0) before and after the Kaikoura earthquake, respectively. Star denotes the epicenter of the mainshock. K: Kaikoura, B: Blenheim. A broken circle denotes the approximate area of relatively high velocity (> about 5 km/s). (b) Map view of Vp at a depth of 16 km. A broken circle denotes the approximate area of relatively high velocity (> about 6 km/s). (c) Satellite image. Red line denotes surface traces of active fault. (d) Shaded image of topography. Red lines denote surface traces of active faults. (c) and (d) from the New Zealand Active Fault Database, GNS Science (2021). (For interpretation of the references to colour in this figure legend, the reader is referred to the web version of this article.)

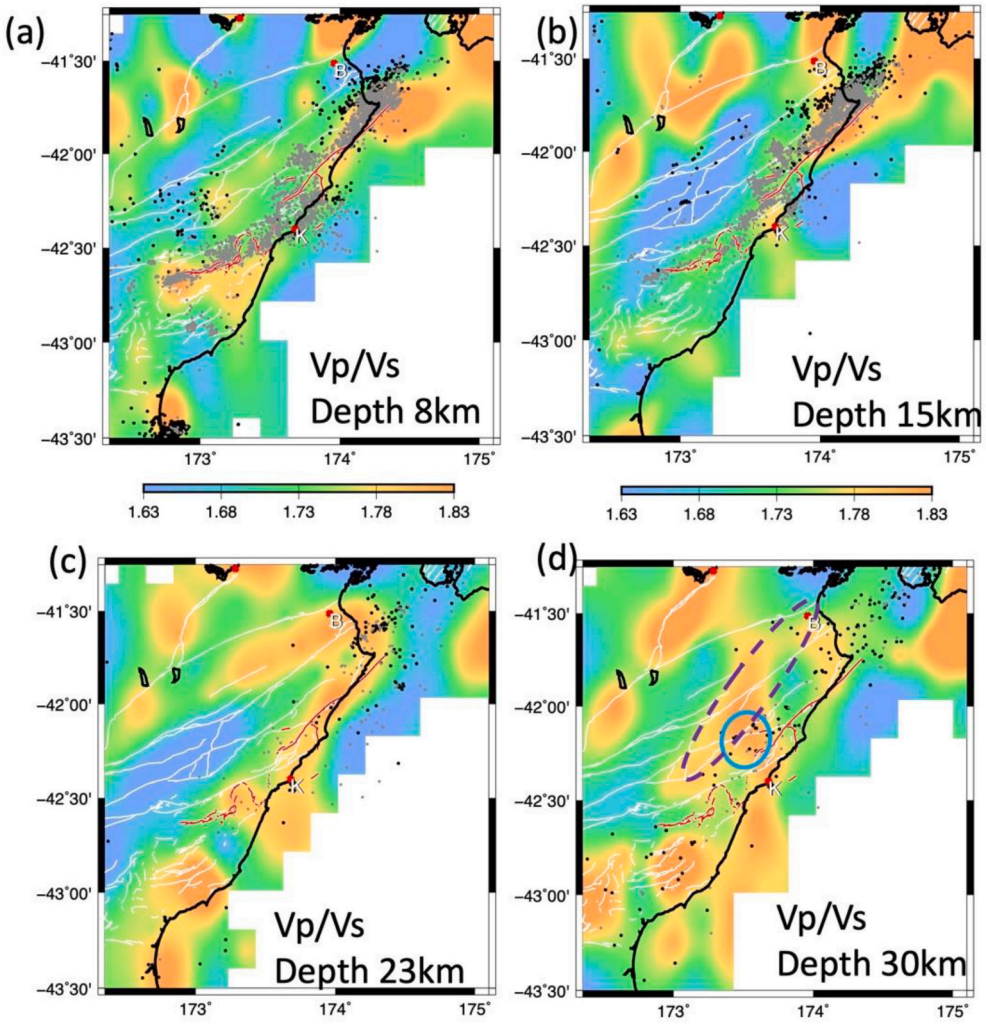

Fig. 8. Map views of Vp/Vs at a depth of (a) 8 km, (b) 15 km, (c) 23 km, and (d) 30 km. White and red lines denote surface traces of active faults and coseismic faults, respectively. Grey and black dots are the earthquakes within 3 km of the map slice before and after the Kaikoura earthquake, respectively. Star denotes the epicenter of the mainshock. Blue circle shows in (d) approximate area of large coseismic slip from Hamling et al. (2017). Purple and broken-line circle in (d) shows approximate area of large postseismic slip from Wallace et al. (2018). (For interpretation of the references to colour in this figure legend, the reader is referred to the web version of this article.)

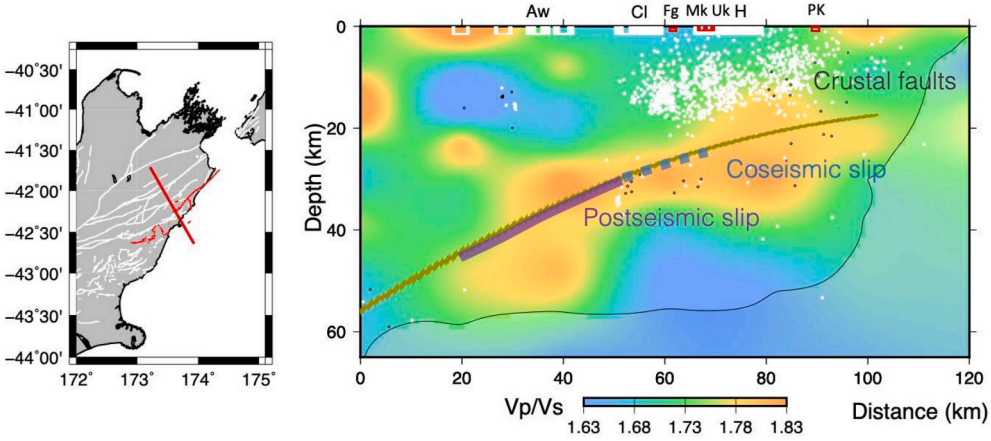

Fig. 9. Cross-section of Vp/Vs across the Kaikoura Peninsula. The resolved area is shown by the black line. Blue broken and purple bold lines show approximate locations of possible coseismic slip (Hamling et al., 2017) and postseismic slip (Wallace et al., 2018) on the plate interface, respectively. (For interpretation of the references to colour in this figure legend, the reader is referred to the web version of this article.)

is apparent beneath the aftershock area and along the plate interface of the subducted Pacific plate.

The selection of an adequate initial model is important for obtaining a reliable seismic velocity structure by seismic tomography because the inversion process is done iteratively from the initial model (e.g., Kissling et al., 1994). In this case, we used the Eberhart-Phillips et al. (2010) model as the adequate initial model in the study area. However, even if we used a one-dimensional model as the initial model, the result was similar to that from the original initial model. For example, high Vp/Vs is seen beneath the aftershock area and along the plate interface of the subducted Pacific plate (Fig. S6), although with less amplitude of perturbation.

4. Discussion

4.1. The aftershock distribution

The observed complexities in the aftershock distribution show the multi-fault rupture character of the Kaikōura earthquake. Similar to the surface fault distribution, the seismic velocity structure and aftershock distribution also show complex structure through the rupture area. Our hypocenter distribution shows aftershock alignments similar to those obtained by previous studies (e.g., Chamberlain et al., 2021; for example, compare Fig. 5 with Fig. 6(e) in this study). From cross-sections, the aftershock distribution is consistent with some aspects of the fault models in previous studies (e.g., Hamling et al., 2017; Mouslopoulou et al., 2019), although there are also some discrepancies between them. We found many aftershocks have occurred off the co-seismic faults. These off-fault aftershocks could be caused by the stress disturbance by the mainshock rupture (e.g., Matsuno et al., 2022). However, the deeper extent of the geodetically estimated co-seismic rupture (deeper than 20 km in Fig. 6 a-f, i-l) than the depth extent of the aftershocks (shallower than 20 km) is difficult to reconcile, although this shallower cut-off depth of aftershocks may suggest a deeper extent of aseismic slip just after the coseismic slip. It suggests the need for a re-examination of fault structure and co-seismic slip distribution with consideration of the aftershock distribution.

4.2. Vp distribution

In the entire focal area, the seismic velocity structure is laterally variable. Some of the lateral variations can be interpreted using surface geology. In the uppermost crust (Fig. 7 (a)), lower velocities (Vp $<$ 4 km/s) occur beneath the basins in Emu Plain and at Cape Campbell. This lower velocity likely corresponds to a sedimentary layer that is thicker in the basins, as shown in the cross-sections (Fig. 3). The higher crustal velocity region (Vp $>$ 5 km/s) surrounding these lower velocities generally indicates the Marlborough basement terranes (Fig. 2). In particular, the higher crustal velocity region near Kaikōura in Fig. 5 (d) and (e) and Fig. 7 (a) and (b) is very interesting for considering the rupture process of the mainshock. Aki (1979) proposed the barrier concept for stopping an earthquake rupture. An example was the southern end of the 1906 San Francisco earthquake, where a higher seismic velocity area is observed. A similar high-velocity body was found at the eastern end of the 2010–2011 Darfield-Christchurch earthquake sequence (Reyners et al., 2013). They interpreted the high-velocity body as a “strong basalt plug” under Banks Peninsula. In the case of the 2016 Kaikoura earthquake, the rupture extended eastward from the hypocenter, but, near the Kaikoura Peninsula, it turned northeastward, and several short-length faults were ruptured. If the higher crustal velocity region near Kaikōura is a stronger area compared with the surrounding, the higher velocity area may have acted as a barrier that discouraged eastward rupture from the hypocenter and led to the complex slip distribution in this area.

In this study, we used regular gridding with a horizontal distance of 20 km. This grid is coarser than that used in Eberhart-Phillips et al. (2010). Thus, the initial and final models in this study are smoother. From the checkerboard test, we decided it was difficult to determine the seismic velocity structure using a finer grid in the surrounding area of the Kaikoura earthquake. This is caused by a limited distribution of hypocenters, most of which are the aftershocks of the Kaikoura earthquake, and a sparse distribution of the stations. A finer structure can be obtained in future studies e.g. if data from our temporary stations are merged with that of Eberhart-Phillips et al. (2010).

4.3. Vp/Vs distribution

Our tomography results show that high Vp/Vs ratios below the aftershock area in the middle to lower crust occurs not only around the hypocenter but also along the northern part of the rupture zone. This high Vp/Vs zone is narrower (about 20 km wide) than in previous studies (about 50 km wide) (Eberhart-Phillips and Bannister, 2010; Okada et al., 2019) and the spatial correlation with the aftershock distribution has become clearer.

The geology of the rupture zone is highly varied within the upper 5 km of the crust. It is comprised of a folded and faulted Tertiary succession of sedimentary strata and volcanics unconformably overlying a composite basement made up of a complex mixture of deformed Triassic-Cretaceous terranes (Rakaia, Pahau, Esk Head belt, etc.), all of which were intruded by the Tapuaenuku mafic-ultramafic igneous complex of mid- to late-Cretaceous age (Rattenbury et al., 2006). Mafic-ultramafic igneous rocks have a high Poisson’s ratio and high Vp/Vs (e.g. Christensen, 1996). The middle to deeper crustal geology likely includes higher metamorphic grade equivalents of the composite terrane assemblage, as discussed by Eberhart-Phillips and Bannister (2010). Thus, some of the high Vp/Vs anomalies might be interpreted in terms of geology.

Fluid overpressure is another possible cause of high Vp/Vs anomalies. For the continental crust, average Vp/Vs is 1.77, which corresponds to average Poisson’s ratio of 0.265 (e.g., Christensen, 1996). An increase of pore-fluid pressure to near-lithostatic pressure would cause strong interconnectivity of pore fluid and increase Vp/Vs (e.g., Nur, 1972; Takei, 2002). Regions with Vp/Vs $>$ 1.80 are thus potentially fluid overpressured. We note that the area of the Kaikōura earthquake has a transpressional deformation character, with active deformation combining thrusting and dextral strike-slip. Under the transpressional deformation, local loading to failure is generally likely to be load-strengthening where, as shear stress is increasing, the mean stress is also rising so that pore-fluid pressure also increases under some conditions (e.g., if pores are closed), contributing to lower effective normal stress on potential faults (e.g., Sibson, 1991; Sibson, 1993).

Additionally, fluid is abundantly supplied by the circulation that is caused by the plate subduction. Wannamaker et al. (2009); (see Fig. 1 for reference) found low electrical resistivity zone (which they termed the A zone) beneath the Marlborough faults, including the area of the hypocenter of the Kaikōura earthquake. Wannamaker et al. (2009) suggest the origin of the A zone is dewatering from sediment, including the dehydration of the clay to mica transition (100–180° C) (Peacock, 2003) on the subducted plate interface. The spatial variations of Vp/Vs shown in this study might be caused by the distribution of subducted sediment and the temperature distribution. Matsumoto et al. (2020) found seismic reflectors below the aftershock area. These seismic reflectors could be fracture veins formed by overpressured fluids during fault valve activity (e.g., Sibson, 1992). The existence of the high Vp/Vs area with low electrical resistivity zone and seismic reflectors suggests overpressured fluid in and beneath the focal area. Overpressured fluid decreases effective normal stress and shear strength. Spatial correlation between rupture areas and high Vp/Vs suggests the involvement of overpressured fluid in the nucleation and propagation of rupture segments of the 2016 Kaikōura earthquake (e.g., Sibson, 2020).

The maximum horizontal stress direction is about N110E both before and after the Kaikōura earthquake (Balfour et al., 2005; Sibson et al.,

2012; Townend et al., 2012; Matsuno et al., 2022; Graham et al., 2020). The involvement of overpressured fluid is also supported by the reactivation of unfavourably oriented strike-slip ruptures, many lying at c. 70° to the regional maximum compressive stress trajectories (e.g., Sibson, 1990; Matsuno et al., 2022). Sibson (1990) proposed the fault-valve hypothesis. Some of the fluids in the crust originate from the deep area, e.g., the water dehydrated from the subducted plate. The existence of an impermeable barrier, which is formed by hydrothermal deposition of silicate minerals and sealing, raises fluid pressure beneath it, in some cases reaching near lithostatic pressure. The high Vp/Vs areas we found would suggest these overpressured fluids are present in and around the focal area.

This overpressured fluid causes a reduction in the frictional strength of the fault and triggers the earthquake. We note that damage on faults is often considered when velocity changes after earthquakes. Whereas isotropic velocity changed with time near the faults (Madley et al., 2022), the changes were only on the order of 0.5%, lower than the differences up to 10% that we measure between the high- and low-Vp/Vs regions. Furthermore, the damage did not seem to affect the crack orientations or abundance that could cause macroscopic Vp/Vs changes, since neither the shear-wave splitting fast directions nor delay times changed after the mainshock (Graham et al., 2020). Therefore, we discount co-Kaikoura earthquake fault damage as the cause of the high Vp/Vs anomalies observed in this study. But, fault damage accumulated in the long-term by repetitive rupture (e.g., Sibson, 2003, Yukutake and Iio, 2017) may result in high Vp/Vs anomalies if overpressured fluid exists in the fault damage zone as discussed in the previous paragraph.

Hamling et al. (2017) showed that the large compensated linear vector dipole (CLVD) component was included in the total moment tensor. The large CLVD component may suggest the tensile crack opening caused by fluid migration, which triggered the co- and post-seismic ruptures of the 2016 Kaikoura earthquake. (e.g., Vavryčuk, 2002).

We also found high Vp/Vs anomalies below the crust on and around the subducted plate interface. At a depth of 20–50 km (Fig. 9), the location of possible coseismic slip (Hamling et al., 2017) and afterslip (Wallace et al., 2018; Yu et al., 2020) of the Kaikōura earthquake on the plate interface roughly corresponds to a high Vp/Vs area along with the interface and above the Pacific Plate. A similar example of a high Vp/Vs anomalous area was seen at a depth of about 30 km along the source area of low-frequency tremor (LFT) and slow slip earthquakes (SSE) in the Nankai Trough subduction zone, SW Japan (e.g., Shelly et al., 2006). Sibson (2017) suggested that low permeability seals within the subduction interface shear zone could exist, which would increase the pore-fluid pressure, and increase Vp/Vs. These high Vp/Vs zones around the plate interface may indicate that high pore-fluid pressure promotes slip on the plate interface.

5. Conclusions

We have carried out seismic velocity tomography in the rupture area of the 2016 Kaikōura earthquake using data from temporary and permanent seismic networks. We obtained detailed models of the seismic velocity structure and aftershock distribution of the earthquake.

The tomographic image with the precise aftershock distribution shows the complexity of the 2016 Kaikōura earthquake. Details are as follows: In the epicentral area of the Humps West fault, the aftershocks are distributed at the northern margin of the Emu Plain, which is shown as a thick near-surface layer with a low seismic velocity (Fig. 3). The aftershock alignment is reasonably consistent with the geometry of the corresponding sub-fault, although slip at a depth greater than the 20 km maximum earthquake depth is estimated by the Hamling et al. (2017) model. In the Kaikōura area (Fig. 6), the aftershocks are distributed within a high-velocity area. In the inland Kaikōura area along with the southern Jordan Thrust and nearby areas, the aftershocks form some small clusters (Fig. 7). In the Kekerengu area (Fig. 8), the aftershocks are distributed at the western margin of the coastal area. The aftershocks are distributed in an alignment whose dip is shallower than the fault model.

A higher crustal velocity region is present near Kaikōura. This high-velocity body may have acted as a barrier that discouraged eastward rupture from the hypocenter and led to the complex fault distribution.

We found high Vp/Vs along the faults of the 2016 Kaikōura earthquake, and the plate interface where the afterslip occurred. The existence of high Vp/Vs suggests overpressured fluid promotes the occurrence of the multi-fault rupture of the Kaikōura earthquake and its afterslip.

CRediT authorship contribution statement

Tomomi Okada: Conceptualization, Data curation, Formal analysis, Investigation, Methodology, Visualization, Writing – original draft. **Miu Matsuno:** Conceptualization, Data curation, Investigation, Writing – review & editing. **Satoshi Matsumoto:** Conceptualization, Data curation, Investigation, Supervision, Writing – review & editing. **Yuta Kawamura:** Conceptualization, Data curation, Investigation, Writing – review & editing. **Yoshihisa Iio:** Conceptualization, Data curation, Funding acquisition, Project administration, Supervision, Writing – review & editing. **Tadashi Sato:** Conceptualization, Data curation, Investigation. **Ayaka Tagami:** Conceptualization, Writing – review & editing. **Satoshi Hirahara:** Data curation. **Shuutoku Kimura:** Data curation. **Stephen Bannister:** Conceptualization, Data curation, Supervision, Writing – review & editing. **John Ristau:** Conceptualization, Investigation, Writing – review & editing. **Martha K. Savage:** Conceptualization, Data curation, Supervision, Writing – review & editing. **Clifford H. Thurber:** Conceptualization, Data curation, Supervision, Writing – review & editing. **Richard H. Sibson:** Conceptualization, Data curation, Supervision, Writing – review & editing.

Declaration of competing interest

The authors declare that they have no known competing financial interests or personal relationships that could have appeared to influence the work reported in this paper.

Data availability

The data that support the findings of this study are available from the corresponding author, Tomomi Okada, upon reasonable request. Some outcomes of this paper will be announced on the corresponding author's website (https://www.aob.gp.tohoku.ac.jp/~okada).

Acknowledgments

This study was supported by the Ministry of Education, Culture, Sports, Science, and Technology (MEXT) of Japan, under its Observation and Research Program for Prediction of Earthquakes and Volcanic Eruptions. This work was also conducted with the support of a Grant-in-Aid for Special Purposes (15H05206), Japan Society for the Promotion of Science, Japan, and with funding from the New Zealand Earthquake Commission projects 18/753 and 18/755 and the US National Science Foundation awards EAR-1717119 and EAR-1756075. This work was partly conducted with the support of the Scientific Research Program on Innovative Areas, "Crustal Dynamics" at the Kyoto University (2608), Japan Society for the Promotion of Science, Japan. We acknowledge the New Zealand GeoNet programme and its sponsors EQC, GNS Science, LINZ, NEMA and MBIE for providing data/images used in this study. The authors have declared no conflicts of interest.

We gratefully acknowledge the many farming communities in Nelson, Marlborough, and Canterbury who allowed access to their land and the installation of seismic stations, and the Department of Conservation for granting access to Molesworth Station. Southern Geophysical Ltd. Maintained and serviced the field seismic stations. Home

Seismometer Corporation (Dr. Shigeki Horiuchi) contributed to waveform data processing.

The program codes of the double-difference tomography series are kindly provided by Haijiang Zhang. We acknowledge the efforts towards seismic observation by M. Reyners, J. Pettinga, F. Ghisetti, T. Miura, M. Kosuga, S. Ohmi, Y. Fukahata, Y. Takada, Y. Hamada, M. Nakamoto, T. Nakayama, M. Suzuki, K. Tateiwa, and I. Yoneda.

Finally, we are grateful to the referee and the reviewers for useful comments.

Appendix A. Supplementary data

Supplementary data to this article can be found online at https://doi.org/10.1016/j.pepi.2024.107155.

References

Aki, K., 1979. Characterization of barriers on an earthquake fault. J. Geophys. Res. 84, 6140. https://doi.org/10.1029/JB084iB11p06140.

Ando, R., Kaneko, Y., 2018. Dynamic rupture simulation reproduces spontaneous multifault rupture and arrest during the 2016 M w 7.9 Kaikōura earthquake. Geophys. Res. Lett. 2018GL080550 https://doi.org/10.1029/2018GL080550.

Bai, Y., Lay, T., Cheung, K.F., Ye, L., 2017. Two regions of seafloor deformation generated the tsunami for the 13 November 2016, Kaikōura, New Zealand earthquake. Geophys. Res. Lett. 44, 6597–6606. https://doi.org/10.1002/2017GL073717.

Balfour, N.J., Savage, M.K., Townend, J., 2005. Stress and crustal anisotropy in Marlborough, New Zealand: evidence for low fault strength and structure-controlled anisotropy. Geophys. J. Int. 163, 1073–1086. https://doi.org/10.1111/j.1365-246X.2005.02783.x.

Cesca, S., Zhang, Y., Mouslopoulou, V., Wang, R., Saul, J., Savage, M., Heimann, S., Kufner, S.-K., Oncken, O., Dahm, T., 2017. Complex rupture process of the mw 7.8, 2016, Kaikōura earthquake, New Zealand, and its aftershock sequence. Earth Planet. Sci. Lett. 478, 110–120. https://doi.org/10.1016/j.epsl.2017.08.024.

Chamberlain, C.J., Frank, W.B., Lanza, F., Townend, J., Warren-Smith, E., 2021. Illuminating the pre-, co-, and post-seismic phases of the 2016 M7. 8 Kaikōura earthquake with 10 years of seismicity. J. Geophys. Res. Solid Earth 126 (8) e2021JB022304.

Christensen, N.I., 1996. Poisson's ratio and crustal seismology. J. Geophys. Res. 101, 3139. https://doi.org/10.1029/95JB03446.

Clark, K.J., Nissen, E.K., Howarth, J.D., Hamling, I.J., Mountjoy, J.J., Ries, W.F., Jones, K., Goldstien, S., Cochran, U.A., Villamor, P., Hreinsdóttir, S., Litchfield, N.J., Mueller, C., Berryman, K.R., Strong, D.T., 2017. Highly variable coastal deformation in the 2016 M W 7.8 Kaikōura earthquake reflects rupture complexity along a transpressional plate boundary. Earth Planet. Sci. Lett. https://doi.org/10.1016/j.epsl.2017.06.048.

Eberhart-Phillips, D., Bannister, S., 2010. 3-D imaging of Marlborough, New Zealand, subducted plate and strike-slip fault systems. Geophys. J. Int. 182, 73–96. https://doi.org/10.1111/j.1365-246X.2010.04621.x.

Eberhart-Phillips, D., Michael, A.J., 1993. Three-dimensional velocity structure, seismicity, and fault structure in the Parkfield region, Central California. J. Geophys. Res. 98, 15737. https://doi.org/10.1029/93JB01029.

Eberhart-Phillips, D., Michael, A.J., 1998. Seismotectonics of the Loma Prieta, California, region determined from three-dimensional V p, V p / V s, and seismicity. J. Geophys. Res. Solid Earth 103, 21099–21120. https://doi.org/10.1029/98JB01984.

Eberhart-Phillips, D., Reyners, M., Bannister, S., Chadwick, M., Ellis, S., 2010. Establishing a versatile 3-D seismic velocity model for New Zealand. Seismol. Res. Lett. 81, 992–1000. https://doi.org/10.1785/gssrl.81.6.992.

GNS Science, 2021. New Zealand Active Faults Database [WWW Document]. URL. https://data.gns.cri.nz/af/ (accessed 3.3.21).

GNS Science, 2023a. GeoNet Aotearoa New Zealand earthquake catalogue [dataset]. GNS Sci. GeoNet. https://doi.org/10.21420/0S8P-TZ38.

GNS Science, 2023b. GeoNet Aotearoa New Zealand earthquake moment tensor solutions [dataset]. GNS Sci. GeoNet. https://doi.org/10.21420/MMJ9-CZ67.

Graham, K.M., Savage, M.K., Arnold, R., Zal, H.J., Okada, T., Iio, Y., Matsumoto, S., 2020. Spatio-temporal analysis of seismic anisotropy associated with the Cook Strait and Kaikōura earthquake sequences in New Zealand. Geophys. J. Int. 223, 1987–2008. https://doi.org/10.1093/gji/ggaa433.

Hamling, I.J., Hreinsdóttir, S., Clark, K., Elliott, J., Liang, C., Fielding, E., Litchfield, N., Villamor, P., Wallace, L., Wright, T.J., D'Anastasio, E., Bannister, S., Burbidge, D., Denys, P., Gentle, P., Howarth, J., Mueller, C., Palmer, N., Pearson, C., Power, W., Barnes, P., Barrell, D.J.A., Van Dissen, R., Langridge, R., Little, T., Nicol, A., Pettinga, J., Rowland, J., Stirling, M., 2017. Complex multifault rupture during the 2016 M w 7.8 Kaikōura earthquake, New Zealand. Science 356. https://doi.org/10.1126/science.aam7194 eaam7194.

Heath, B., Eberhart-Phillips, D., Lanza, F., Thurber, C., Savage, M., Okada, T., Matsumoto, S., Iio, Y., Bannister, S., 2022. Fracturing and pore-fluid distribution in the Marlborough region, New Zealand from body-wave tomography: implications for regional understanding of the Kaikōura area. Earth Planet. Sci. Lett. 593, 117666 https://doi.org/10.1016/j.epsl.2022.117666.

Horiuchi, S., Matsuzawa, T., Hasegawa, A., 1992. A real-time processing system of seismic wave using personal computers. J. Phys. Earth 40, 395–406. https://doi.org/10.4294/jpe1952.40.395.

Kawamura, Y., Matsumoto, S., Okada, T., Matsuno, M., Iio, Y., Sato, T., Bannister, S., Ristau, J., Savage, M.K., Sibson, R.H., 2021. Characteristic of fault geometry and the subducting plate boundary in the focal area of the 2016 Mw7.8 Kaikōura earthquake, New Zealand inferred from high precision aftershock distribution. In: Japan Geoscience Union Meeting.

Kissling, E., Ellsworth, W.L., Eberhart-Phillips, D., Kradolfer, U., 1994. Initial reference models in local earthquake tomography. J. Geophys. Res. 99, 19635. https://doi.org/10.1029/93JB03138.

Lamb, S., Arnold, R., Moore, J.D.P., 2018. Locking on a megathrust as a cause of distributed faulting and fault-jumping earthquakes. Nat. Geosci. 11, 871–875. https://doi.org/10.1038/s41561-018-0230-5.

Lanza, F., Chamberlain, C.J., Jacobs, K., Warren-Smith, E., Godfrey, H.J., Kortink, M., Thurber, C.H., Savage, M.K., Townend, J., Roecker, S., Eberhart-Phillips, D., 2019. Crustal fault connectivity of the Mw 7.8 2016 Kaikōura earthquake constrained by aftershock relocations. Geophys. Res. Lett. 2019GL082780 https://doi.org/10.1029/2019GL082780.

Litchfield, N.J., Villamor, P., van Dissen, R.J., Nicol, A., Barnes, P.M., Barrell, D.J.A., Pettinga, J.R., Langridge, R.M., Little, T.A., Mountjoy, J.J., Ries, W.F., Rowland, J., Fenton, C., Stirling, M.W., Kearse, J., Berryman, K.R., Cochran, U.A., Clark, K.J., Hemphill-Haley, M., Khajavi, N., Jones, K.E., Archibald, G., Upton, P., Asher, C., Benson, A., Cox, S.C., Gasston, C., Hale, D., Hall, B., Hatem, A.E., Heron, D.W., Howarth, J., Kane, T.J., Lamarche, G., Lawson, S., Lukovic, B., McColl, S.T., Madugo, C., Manousakis, J., Noble, D., Pedley, K., Sauer, K., Stahl, T., Strong, D.T., Townsend, D.B., Toy, V., Williams, J., Woelz, S., Zinke, R., 2018. Surface rupture of multiple crustal faults in the 2016 Mw 7.8 Kaikōura, New Zealand, earthquake. Bull. Seismol. Soc. Am. 108, 1496–1520. https://doi.org/10.1785/0120170300.

Little, T.A., Van Dissen, R., Kearse, J., Norton, K., Benson, A., Wang, N., 2018. Kekerengu fault, New Zealand: timing and size of late Holocene surface ruptures. Bull. Seismol. Soc. Am. 108, 1556–1572. https://doi.org/10.1785/0120170152.

Madley, M., Savage, M.K., Yates, A., Wang, W., Okada, T., Matsumoto, S., Iio, Y., Jacobs, K., 2022. Velocity changes around the Kaikōura earthquake ruptures from ambient noise cross-correlations. Geophys. J. Int. https://doi.org/10.1093/gji/ggab514/6479127.

Matsumoto, S., Kawamura, Y., Okada, T., Matsuno, M., Iio, Y., Sibson, R.H., Savage, M. K., Graham, K.M., Suzuki, M., Bannister, S., 2020. S-wave reflectors and aftershock activity in the 2016 Kaikōura, New Zealand earthquake hypocentral area. In: JpGU-AGU Joint Meeting. SSS11-03.

Matsuno, M., Tagami, A., Okada, T., Matsumoto, S., Kawamura, Y., Iio, Y., Sato, T., Nakayama, T., Hirahara, S., Bannister, S., Ristau, J., Savage, M.K., Thurber, C.H., Sibson, R.H., 2022. Spatial and temporal stress field changes in the focal area of the 2016 Kaikōura earthquake, New Zealand: a multi-fault process interpretation. Tectonophysics 835, 229390. https://doi.org/10.1016/j.tecto.2022.229390.

Mouslopoulou, V., Saltogianni, V., Nicol, A., Oncken, O., Begg, J., Babeyko, A., Cesca, S., Moreno, M., 2019. Breaking a subduction-termination from top to bottom: The large 2016 Kaikōura Earthquake, New Zealand. Earth Planet. Sci. Lett. 506, 221–230. https://doi.org/10.1016/j.epsl.2018.10.020.

Nicol, A., Khajavi, N., Pettinga, J.R., Fenton, C., Stahl, T., Bannister, S., Pedley, K., Hyland-Brook, N., Bushell, T., Hamling, I., Ristau, J., Noble, D., McColl, S.T., 2018. Preliminary geometry, displacement, and kinematics of fault ruptures in the Epicentral region of the 2016 mw 7.8 Kaikōura, New Zealand, Earthquake. Bull. Seismol. Soc. Am. 108, 1521–1539. https://doi.org/10.1785/0120170329.

Nur, A., 1972. Dilatancy, pore fluids, and premonitory variations of ts/tp travel times. Bull. Seismol. Soc. Am. 62, 1217–1222.

Okada, T., Hasegawa, A., Suganomata, J., Zhao, D., Zhang, H., Thurber, C., 2007. Imaging the source area of the 1995 southern Hyogo (Kobe) earthquake (M7.3) using double-difference tomography. Earth Planet. Sci. Lett. 253, 143–150. https://doi.org/10.1016/j.epsl.2006.10.022.

Okada, T., Umino, N., Hasegawa, A., 2012. Hypocenter distribution and heterogeneous seismic velocity structure in and around the focal area of the 2008 Iwate-Miyagi Nairiku earthquake, NE Japan—possible seismological evidence for a fluid driven compressional inversion earthquake. Earth Planets Sp. 64, 717–728. https://doi.org/10.5047/eps.2012.03.005.

Okada, T., Iio, Y., Matsumoto, S., Bannister, S., Ohmi, S., Horiuchi, S., Sato, T., Miura, T., Pettinga, J., Ghisetti, F., Sibson, R.H., 2019. Comparative tomography of reverse-slip and strike-slip seismotectonic provinces in the northern South Island, New Zealand. Tectonophysics 765, 172–186. https://doi.org/10.1016/j.tecto.2019.03.016.

Peacock, S.M., 2003. Thermal structure and metamorphic evolution of subducting slabs. Geophys. Monogr. 138, 7–22. https://doi.org/10.1029/138GM02.

Rattenbury, M., Townsend, D.B., Johnston, M., 2006. Geology of the Kaikōura area. In: IGNS 1250,000 Geol. Map 13.

Reyners, M., Eberhart-Phillips, D., Martin, S., 2013. Prolonged Canterbury earthquake sequence linked to widespread weakening of strong crust. Nat. Geosci. 7, 34–37. https://doi.org/10.1038/ngeo2013.

Ruina, A., 1983. Slip instability and state variable friction laws. J. Geophys. Res. Solid Earth 88, 10359–10370. https://doi.org/10.1029/JB088iB12p10359.

Shelly, D.R., Beroza, G.C., Ide, S., Nakamura, S., 2006. Low-frequency earthquakes in Shikoku, Japan, and their relationship to episodic tremor and slip. Nature 442, 188–191. https://doi.org/10.1038/nature04931.

Shito, A., Matsumoto, S., Shimizu, H., Ohkura, T., Takahashi, H., Sakai, S., Okada, T., Miyamachi, H., Kosuga, M., Maeda, Y., Yoshimi, M., Asano, Y., Okubo, M., 2017. Seismic velocity structure in the source region of the 2016 Kumamoto earthquake sequence, Japan. Geophys. Res. Lett. 44, 7766–7772. https://doi.org/10.1002/2017GL074593.

Sibson, R.H., 1990. Rupture nucleation on unfavorably oriented faults. Bull. Seismol. Soc. Am. 80, 1580–1604.
Sibson, R.H., 1991. Loading of faults to failure. Bull. Seismol. Soc. Am. 81, 2493–2497.
Sibson, R.H., 1992. Implications of fault-valve behaviour for rupture nucleation and recurrence. Tectonophysics 211, 283–293. https://doi.org/10.1016/0040-1951(92)90065-E.
Sibson, R.H., 1993. Load-strengthening versus load-weakening faulting. J. Struct. Geol. 15, 123–128. https://doi.org/10.1016/0191-8141(93)90090-W.
Sibson, R.H., 2003. Thickness of the seismic slip zone. Bull. Seismol. Soc. Am. 93, 1169–1178. https://doi.org/10.1785/0120020061.
Sibson, R.H., 2017. Tensile overpressure compartments on low-angle thrust faults. Earth Planets Sp. 69, 113. https://doi.org/10.1186/s40623-017-0699-y.
Sibson, R.H., 2020. Preparation zones for large crustal earthquakes consequent on fault-valve action. Earth Planets Sp. 72, 31. https://doi.org/10.1186/s40623-020-01153-x.
Sibson, R.H., Ghisetti, F.C., Crookbain, R., 2012. Andersonian wrench faulting in a regional stress field during the 2010-2011 Canterbury, New Zealand, earthquake sequence. Geol. Soc. London Spec. Publ. 367, 7–18. https://doi.org/10.1144/SP367.2.
Takei, Y., 2002. Effect of pore geometry on V P / V S : from equilibrium geometry to crack. J. Geophys. Res. 107, 2043. https://doi.org/10.1029/2001JB000522.
Townend, J., Sherburn, S., Arnold, R., Boese, C., Woods, L., 2012. Three-dimensional variations in present-day tectonic stress along the Australia–Pacific plate boundary in New Zealand. Earth Planet. Sci. Lett. 353–354, 47–59. https://doi.org/10.1016/j.epsl.2012.08.003.
Van Dissen, R., Yeats, R.S., 1991. Hope fault, Jordan thrust, and uplift of the seaward Kaikōura range, New Zealand. Geology 19, 393. https://doi.org/10.1130/0091-7613(1991)019<0393:HFJTAU>2.3.CO;2.
Vavryčuk, V., 2002. Non-double-couple earthquakes of 1997 January in West Bohemia, Czech Republic: evidence of tensile faulting. Geophys. J. Int. 149, 364–373. https://doi.org/10.1046/j.1365-246X.2002.01654.x.
Waldhauser, F., 2001. hypoDD - a program to compute double-difference hypocenter locations. USGS Open-File Rep. 113 https://doi.org/10.3133/ofr01113.
Waldhauser, F., Ellsworth, B., 2000. A double-difference earthquake location algorithm: method and application to the northern Hayward fault, California. Bull. Seismol. Soc. Am. 90, 1353–1368. https://doi.org/10.1785/0120000006.
Wallace, L.M., Barnes, P., Beavan, J., Van Dissen, R., Litchfield, N., Mountjoy, J., Langridge, R., Lamarche, G., Pondard, N., 2012. The kinematics of a transition from subduction to strike-slip: an example from the Central New Zealand plate boundary. J. Geophys. Res. 117, B02405. https://doi.org/10.1029/2011JB008640.
Wallace, L.M., Hreinsdóttir, S., Ellis, S., Hamling, I., D'Anastasio, E., Denys, P., 2018. Triggered slow slip and Afterslip on the southern Hikurangi subduction zone following the Kaikōura earthquake. Geophys. Res. Lett. https://doi.org/10.1002/2018GL077385.
Wannamaker, P.E., Caldwell, T.G., Jiracek, G.R., Maris, V., Hill, G.J., Ogawa, Y., Bibby, H.M., Bennie, S.L., Heise, W., 2009. Fluid and deformation regime of an advancing subduction system at Marlborough, New Zealand. Nature 460, 733–736. https://doi.org/10.1038/nature08204.
Weaver, K.C., Cox, S.C., Townend, J., Rutter, H., Hamling, I.J., Holden, C., 2019. Seismological and hydrogeological controls on New Zealand-wide groundwater level changes induced by the 2016 M w 7.8 Kaikōura earthquake. Geofluids 2019, 1–18. https://doi.org/10.1155/2019/9809458.
Williams, C.A., Eberhart-Phillips, D., Bannister, S., Barker, D.H.N., Henrys, S., Reyners, M., Sutherland, R., 2013. Revised Interface geometry for the Hikurangi subduction zone, New Zealand. Seismol. Res. Lett. 84, 1066–1073. https://doi.org/10.1785/0220130035.
Yu, C., Li, Z., Penna, N.T., 2020. Triggered afterslip on the southern Hikurangi subduction interface following the 2016 Kaikōura earthquake from InSAR time series with atmospheric corrections. Remote Sens. Environ. 251, 112097 https://doi.org/10.1016/j.rse.2020.112097.
Yukutake, Y., Iio, Y., 2017. Why do aftershocks occur? Relationship between mainshock rupture and aftershock sequence based on highly resolved hypocenter and focal mechanism distributions. Earth Planets Sp. 69, 68. https://doi.org/10.1186/s40623-017-0650-2.
Zhang, H., Thurber, C.H., 2003. Double-difference tomography: the method and its application to the Hayward fault, California. Bull. Seismol. Soc. Am. 93, 1875–1889. https://doi.org/10.1785/0120020190.
Zhang, H., Thurber, C., 2006. Development and applications of double-difference seismic tomography. Pure Appl. Geophys. 163, 373–403. https://doi.org/10.1007/s00024-005-0021-y.